

ALMA and VLA observations of emission from the environment of Sgr A*

F. Yusef-Zadeh,^{1*} R. Schödel² M. Wardle³ H. Bushouse⁴ W. Cotton⁵

M. J. Royster¹ D. Kunneriath² D. A. Roberts¹ E. Gallego-Cano²

¹*Department of Physics and Astronomy Northwestern University, Evanston, IL 60208, US*

²*Instituto de Astrofísica de Andalucía (CSIC), Glorieta de la Astronomía S/N, 18008 Granada, Spain*

³*Department of Physics and Astronomy and Research Centre for Astronomy, Astrophysics*

& Astrophotonics, Macquarie University, Sydney NSW 2109, Australia

⁴*Space Telescope Science Institute, Baltimore, MD 21218*

⁵*National Radio Astronomy Observatory, Charlottesville, VA 22903*

6 March 2024

ABSTRACT

We present 44 and 226 GHz observations of the Galactic center within 20'' of Sgr A*. Millimeter continuum emission at 226 GHz is detected from eight stars that have previously been identified at near-IR and radio wavelengths. We also detect a 5.8 mJy source at 226 GHz coincident with the magnetar SGR J1745-29 located 2.39'' SE of Sgr A* and identify a new $2.5'' \times 1.5''$ halo of mm emission centered on Sgr A*. The X-ray emission from this halo has been detected previously and is interpreted in terms of a radiatively inefficient accretion flow. The mm halo surrounds an EW linear feature which appears to arise from Sgr A* and coincides with the diffuse X-ray emission and a minimum in the near-IR extinction. We argue that the millimeter emission is produced by synchrotron emission from relativistic electrons in equipartition with a ~ 1.5 mG magnetic field. The origin of these is unclear but its coexistence with hot gas supports scenarios in which the gas is produced by the interaction of winds either from the fast moving S-stars, the photo-evaporation of low-mass YSO disks or by a jet-driven outflow from Sgr A*. The spatial anti-correlation of the X-ray, radio and mm emission from the halo and the low near-IR extinction provides compelling evidence for an outflow sweeping up the interstellar material, creating a dust cavity within 2'' of Sgr A*. Finally, the radio and mm counterparts to eight near-IR identified stars within $\sim 10''$ of Sgr A* provide accurate astrometry to determine the positional shift between the peak emission at 44 and 226 GHz.

Key words: accretion, accretion disk – black hole physics – Galaxy: centre

1 INTRODUCTION

The nuclear region of our Galaxy coincides with a stellar cluster consisting of an evolved population and a young population of OB and WR stars (Paumard *et al.* 2006; Lu *et al.* 2009) centered on the $4 \times 10^6 M_{\odot}$ black hole Sgr A* (Reid and Brunthaler 2004; Genzel *et al.* 2010; Schödel *et al.* 2014; Boehle *et al.* 2016; Gillsessen *et al.* 2016). Until recently, the young massive stars within 0.5 pc of Sgr A* could only be identified and studied employing

* E-mail: zadeh@northwestern.edu (FYZ)

adaptive optics in the near-IR. Recent high-resolution radio continuum observations detected 318 compact radio sources within the inner 30'' of Sgr A*. The comparison of radio and near-IR data indicate that at least 45 of the compact radio sources coincide with known sources, many of which are massive stars, identified at K_s and L' bands in the near-IR (Yusef-Zadeh et al. 2016).

Thermal radio emission from a mass-losing star arises from spherically-symmetric, wind of fully-ionized gas expanding at its terminal velocity (e.g., Panagia & Felli 1975). Stellar thermal emission at radio wavelengths could also arise from the photospheres of evolved stars in the nuclear cluster. One way to distinguish between these two different populations is to determine their radio spectral index α where the flux density $S_\nu \propto \nu^{-\alpha}$. Photospheric emission has an inverted spectrum with $\alpha \sim 2$ whereas ionized stellar winds from young massive stars typically have a spectrum with $\alpha \sim 0.6$ (Panagia 1973). Previous detection of radio emission from near-IR identified stars in the inner 10'' of Sgr A* (Yusef-Zadeh et al. 2015a) had a limited frequency coverage between 34 and 44 GHz, thus, it was not possible to accurately determine the spectral index. The present 226 GHz and 44 GHz observations present an opportunity to remedy this by determining the spectrum of radio emission and distinguishing between members of the evolved cluster and massive stars in the young cluster.

To measure orbits of stars around Sgr A*, it is necessary to tie radio and near-IR data into astrometric reference frames. The positions of radio stars can provide precise astrometry relative to Sgr A*. The detection of stars at millimeter (mm) wavelengths opens a new window for astrometric calibration as well as examining if there is a shift in the peak position of Sgr A* between radio and mm wavelengths as might be expected, for example if mm emission from a jet was present (Markoff et al. 2007)

Here we present simultaneous ALMA, VLA and VLT observations of the Galactic center and determine the spectral index between 44 and 226 GHz of eight stellar sources identified at H (1.63 μm) band and two nonthermal sources Sgr A* and the magnetar SGR J1745-29. In addition, we determine the peak position of Sgr A* at 226 GHz by registering the accurate positions of near-IR identified stars detected at 44 and 226 GHz and then search for any shifts in position of Sgr A* at 44 and 226 GHz. Finally, the observations presented here show sub-structures associated with Sgr A* and a network of narrow features at radio and mm. We detect a halo of mm emission from the inner 2'' of Sgr A* which coincides with low near-IR extinction. The size of this halo is similar to that detected at X-rays. We suggest that the outflow from the ionized winds of the S stars orbiting Sgr A* are responsible for this emission. We report tentative detection of faint narrow fibrils of radio and mm emission. We interpret these striking features as arising from the interaction of radial outflows from the Galactic center and the atmospheres of mass-losing stars.

2 OBSERVATIONS AND DATA REDUCTION

2.1 Radio and Millimeter Data

The ALMA, VLA¹, and VLT observations were carried out as part of a multi-wavelength observing campaign to monitor the flux variability of Sgr A*. This campaign was led by Spitzer and Chandra, and radio and mm observations were obtained as part of the director's discretionary time given to us to join the observing campaign. Titan was initially used in ALMA observations (project code 2015.A.00021.S.) as the flux calibrator and NRAO 530 was observed periodically to correct for any changes in phase and amplitude as a function of time. The spectral windows were centered at roughly: 216.2 GHz, 218.0 GHz, 231.9 GHz, and 233.7 GHz. Editing and calibration of the data were carried out with OBIT (Cotton 2008) before all the spectral windows were averaged prior to constructing final images. Observations were made on July 12 and 18, 2016 and the images were combined after scaling the variable flux of Sgr A* during the two epochs of observations.

We carried out VLA B-array observations (program 16A-419) in the Q (7mm) and Ka (9mm) bands on July 12 and 18, 2016 at 44 and 34 GHz, respectively. We used the 3-bit system, which provided full polarization in 4 basebands, each 2 GHz wide. Each subband was made up of 64 channels and channels were 2 MHz wide. We used 3C286 to calibrate the flux density scale and used 3C286 and J1733-1304 (aka NRAO530) to calibrate the bandpass and J1744-3116 to calibrate the complex gains. A phase and amplitude self-calibration procedure was applied to all data using the bright radio source Sgr A*. We used OBIT (Cotton 2008) and CASA to construct radio and mm images. The positions of radio stars are determined with respect to the absolute position of Sgr A*. The Ka band data were compromised by bad weather conditions, thus we do not present those observations.

¹ the Karl G. Jansky Very Large Array (VLA) of the National Radio Astronomy Observatory is a facility of the National Science Foundation, operated under a cooperative agreement by Associated Universities, Inc.

2.2 VLT Data

NACO/VLT was used as part of a coordinated observing campaign, as described above. Ten hours of observations were granted but the observations suffered from bad seeing conditions, with the coherence time being mostly $\tau_0 \lesssim 3$ ms and the isoplanatic angle $\theta_0 \approx 1''$ arcsec. Consequently, the Adaptive Optics (AO) performance was mostly poor, with the exception of a few short intervals of good conditions. As is standard for NACO AO observations of the GC, the loop of the AO system was closed on the $K_s \approx 7$ supergiant IRS 7, located about $5.5''$ north of Sgr A*. For this work we use the best data set, which was obtained on 2016 July 12 during UT 04:26 to 04:58. It consists of observations in the H -band with the S27 camera. The exposure time was set to 3 s. We used NACO's cube-mode and obtained 26 sets of 21 exposures each, amounting to a total integration time of 1638 s. Data reduction was standard (sky subtraction, flat-field correction, dead-pixel interpolation) and all the reduced exposures were aligned via the centroid of the star IRS16 C and mean-combined. Stellar positions and fluxes were extracted with the *StarFinder* package (Diolaiti et al. 2000). We also present the extinction map of the inner $30''$ derived from star counts in the near-IR, details of which are explained in Schödel et al. (2010). Foreground stars were removed prior to creating the extinction map, which thus provides a good measure of the column density of the clouds in the Galactic center.

3 RESULTS

3.1 A $2.5'' \times 1.5''$ Emission Halo Centered on Sgr A*

Figure 1a shows the inner $17'' \times 18''$ of Sgr A* at 225 GHz where the brightest portion of the mini-spiral structure associated with the three-arms of the minispiral (Sgr A West) are detected. The N and E arms and the bar to the south of Sgr A* are prominent. The region within a few arcseconds of Sgr A*, outlined schematically by a dashed semi-circle, shows a number of new structures. One is a diffuse halo structure with an elliptical appearance within $2.5'' \times 1.5''$ of Sgr A* with mean flux density of $\sim 0.2 - 0.5$ mJy beam $^{-1}$. The integrated flux is 81 mJy over an area of 9.7 square arcsecond. This diffuse structure has an X-ray counterpart (Wang et al. 2013). Figure 1b shows a composite image of mm and X-ray emitting gas where we note the diffuse X-ray emission is coincident with the mm halo centered on Sgr A*. The NS elongated X-ray structure G359.945–0.044 about $10''$ NW of Sgr A* is a pulsar wind nebula candidate (Wang et al. 2013). Figure 1c shows the composite image of the extinction in the near-IR and the mm emission. The extinction value in the K_s band ($2.17\mu\text{m}$) ranges between 2.3 and 3.2 (Schödel et al. 2010). We note the halo structure has the lowest extinction ~ 2.4 magnitudes compared to the high extinction of ~ 2.9 magnitudes surrounding it. Dark dashed lines to the south of Sgr A* outline the elliptical halo structure bounded by the bar to the south of Sgr A*. We also note the high extinction associated with the N and E arms and the bar of the mini-spiral (Schödel et al. 2010). The extinction map of the mini-spiral shows clearly the complex nature of cold and dense gas that is externally photoionized by the Galactic center radiation field to create the minispiral.

We note a bow-shock-like structure with an extent of $\sim 2''$ to the NE of Sgr A*. The typical surface brightness of this feature is about 0.2 mJy beam $^{-1}$ at 226 GHz. Finally, a EW mm ridge of emission protrudes from Sgr A*. This ridge appears to extend further to the west for several arcseconds before it merges with the continuum emission from the mini-spiral.

A close-up view of the inner $6'' \times 4''$ of Sgr A* is shown in Figure 2a where contours of mm emission are superimposed on 1.5–7 keV X-ray emission. The extended X-ray emission was identified by Wang et al. (2013). This image shows a spatial correlation between mm and X-ray emission. The diffuse X-ray and mm emission from the halo coincide with a region of low extinction. The mm contours show an elliptically-shaped $2.5'' \times 1.5''$ halo of diffuse emission similar to the X-ray morphology. The anti-correlation of high emission and low extinction suggest clearly that the low extinction is caused by an outflow. Figure 2b shows the close-up view of 226 GHz emission from Sgr A* and its vicinity. The elongated EW structure or the linear ridge appears to be associated with Sgr A*. The bow shock feature lies to the eastern edge of the diffuse halo. The bow-shock may indicate where an outflow from Sgr A* interacts with the ISM in the immediate vicinity of Sgr A*." We also note compact sources that coincide with stellar sources, as described below.

3.2 Compact Stellar Sources at 226 GHz

Ten compact sources at 44 and 226 GHz are identified within the inner 10'' of Sgr A*. These sources, labeled on Figures 2b and 3a,b, are used to astrometrically register the mm and near-IR images. As all radio, mm and near-IR data are taken at the same epoch, we identified radio and mm stars from the first ALMA epoch 2016.54 by comparing all three images. ALMA observations detect eight near-IR identified stellar sources at 226 GHz. These stars also have counterparts at 44 GHz. Tables 1 and 2 list Gaussian-fitted positions of 10 radio and mm sources distributed within the inner 10'' of Sgr A* at 44 and 226 GHz. Entries in the columns of Tables 1 and 2 give the source name at 44 and 226 GHz, alternative names in the literature, the RA and Dec, the angular distance from Sgr A* in increasing order, positional accuracy, the size of the source, the peak and integrated intensities. Column 9 of Table 1 gives the spectral index of individual sources between 44 and 226 GHz. The last column provides the comments on individual sources. The positional accuracy is determined from quadrature sum of errors of the right ascension and declination values from 2D Gaussian fits without including absolute astrometric errors. Because the second epoch of ALMA data had a higher spatial resolution, we compared this epoch with the first epoch of VLA observation at 44 GHz to determine the spectral index of all sources except Sgr A*. The spectral index of Sgr A* is estimated from the same epoch data sets. The positions and the sizes of radio sources are determined from background-subtracted Gaussian fit to the individual radio sources.

We note the radio source associated with IRS 21 has a mm counterpart. This young stellar source (Sanchez-Bermudez *et al.* 2014) is comprised of five radio components (Yusef-Zadeh *et al.* 2014) but only one stellar source is identified at H-band. The radio and infrared properties are similar to those of IRS 13N and IRS 13E suggesting that the radio emission arises from the disks of massive YSO candidates in this cluster (Yusef-Zadeh *et al.* 2015b). We also detect mm emission from the Galactic center magnetar, SGR J1745-29 (Kennea *et al.* 2013; Shannon and Johnston 2013; Torne *et al.* 2017). This source was in its quiescent phase before it was identified as an X-ray outburst (Kennea *et al.* 2013). SGR J1745-29 is the closest known pulsar to Sgr A* located 2.4'' from Sgr A*. The detection of a compact radio source was reported at $\alpha, \delta (J2000) = 17^h45^m40^s.16795 \pm 0.00002 - 29^\circ00'29''.74908 \pm 0.00064$ at 44.6 GHz on 2014 February 21 (Yusef-Zadeh *et al.* 2014). Our 44 GHz image shows a plume-like structure to the north of the magnetar. This plume-like feature with an extent of $0.2'' \times 0.5''$ (width \times length) widens to the north with a peak flux density $0.8 \text{ mJy beam}^{-1}$. It does not have a counterpart at $3.8\mu\text{m}$ (Eckart *et al.* 2013) and has no obvious counterpart at 226 GHz. We do not have sufficient data to determine its spectral index. Future polarization and spectral studies of this feature would determine its nature.

The spectral index of Sgr A* $\alpha = 0.56$ listed in Table 1 is steeper than previously determined from snapshot measurements (An *et al.* 2005). The magnetar has a relatively flat spectrum with $\alpha = -0.21$. The mm emission from the magnetar could be due to the combination of pulsed and diffuse shocked emission produced by the interaction of the pulsar outburst with the ISM (Yusef-Zadeh *et al.* 2016). The remaining eight sources are stellar, six of which have spectra consistent with ionized winds. Sources 7 and 8, which coincide with IRS 3 and IRS 7SW, respectively, have a steep optically thick spectrum consistent with photospheric radio emission. Alternative, these steep spectrum sources could also be generated by ionized winds of massive stars with or wind sources with a varying density gradient and geometry (Panagia & Felli 1975). IRS 3 is the brightest and most extended $3.8\mu\text{m}$ Galactic center (Pott *et al.* 2008) stellar source. The asymmetric shape of the IRS 3 envelope may reflect tidal distortion by Sgr A* (Yusef-Zadeh *et al.* 2017).

3.3 Search for Radio and mm Emission from the S stars

There is a cluster of B dwarf stars associated with the S-star cluster within 1'' of Sgr A* (Gillessen *et al.* 2009, 2016; Yelda *et al.* 2010, 2014). The detection of S stars in the radio and mm has been challenging because of the bright and variable source Sgr A* and its frequency dependent angular size due to interstellar scattering. To search for radio emission from stars within 1'' of Sgr A*, we first calculated the positions of the S stars at the epoch of the mm observation on 2016, July 16 by using orbital parameters derived from near-IR observations (Gillessen *et al.* 2016). Table 3 gives the positions of the S cluster members offset from Sgr A* in R.A. and Declination and their corresponding positional uncertainties at the epoch of 2016.54. The expected positions are indicated as crosses in three images, taken within a few days of each other, a $1.6\mu\text{m}$ H-band, 226 GHz and 44 GHz image, as shown in Figures 4a-c, respectively. The S stars are superimposed after astrometric corrections have been applied to the near-IR and mm images. The near-IR stellar sources coincide well with the predicted positions in Figure 4a. Two bright stellar sources S96 and S97 in Figure 4b coincide with IRS 16NE and IRS 16SE, respectively. There are also coincidences between some S stars, such as S83, and mm peaks in Figure 4b. However, there is extended mm emission, and it is not possible to localize mm counterparts to stellar sources, mainly because of the confusing

compact and extended sources. Remarkably, we note a number of 44 GHz sources throughout the inner $3''$ of Sgr A*, as shown in Figure 4c. In particular, S83 and S33 may have radio counterparts within the positional errors at 44 GHz. Similarly, S5 and S14 coincide with peak radio emission at a level of $0.15 \text{ mJy beam}^{-1}$. Proper motion measurements in the radio are needed to establish that they are indeed counterparts to S stars.

We note a number of radio and mm peaks without stellar counterparts in the H band. Radio sources could have counterparts in the L' band where a number of dusty sources or the so-called dusty S cluster objects (DSO/G2) have been detected (Eckart et al. 2014). However, we have neither the proper motion of DSO sources nor an L' band image taken in the same epoch as the data presented here to confirm $3.8\mu\text{m}$ counterparts to radio peaks. A member of this class of objects detected in the L' band is G2 that was the subject of intense observational campaigns as it passed extremely close to the central black hole (Gillessen et al. 2012; Witzel et al. 2014; Pfuhl et al. 2015; Valencia-Schneider et al. 2015). Given the low spatial resolution of our radio and mm observations, we could not search for radio counterparts to G2. The expected position of the G2 cloud is -85 and 80 mas from Sgr A* (Gillessen, private communication) which is smaller than the $222 \times 128 \text{ mas}$ synthesized beam at 44 GHz.

The compact radio and mm sources detected within $2''$ of Sgr A* with no stellar counterparts could be massive young stellar objects (YSOs), similar to radio counterparts of several members of the IRS 13N cluster (Eckart et al. 2013; Yusef-Zadeh et al. 2014, 2015b). In this interpretation, ionized gas is being photo-evaporated from the disks of YSOs by the UV radiation from young and massive stars located between 1 and $10''$ from Sgr A* (Yusef-Zadeh et al. 2014). Future proper motion and spectral measurements of radio and mm sources are critical to determine their nature.

3.4 Dust Cavities near Sgr A*

We also examined the physical relationship between the S stars and a dust cavity centered on Sgr A* that is present in the extinction map of Sgr A West, as shown in Figure 1c (Schödel et al. 2010). Figure 4d shows the inner $4'' \times 3.5''$ of Sgr A* where the largest concentration of S stars is detected in the Sgr A* dust cavity. The dust cavity coincides with the elongated mm halo and excess diffuse X-ray and radio emission, as discussed earlier (see Figures 2a,b and 4b,c). In addition, the correlation of the dust cavity and a halo of enhanced emission at multiple wavelengths suggests an outflow has destroyed or swept the cold and dense material away from Sgr A*. This X-ray filled cavity with minimum extinction provides the strongest evidence for an outflow, the origin of which is discussed in the next section.

A larger view of the near-IR extinction map identifies regions of low and high columns of dust. Figure 5a,b show the inner $13''$ of Sgr A* delineating extinction clouds and 44 GHz radio continuum emission, respectively. We note a cloud that lies along the northwestern extension of the E arm at $\sim -5''$ and $\sim 1''$ W and N of Sgr A*, respectively. The anticorrelation of this dust cavity and a gap in the ionized gas strongly suggest that the dust cavity is associated with the ionized material.

The extinction map shown in Figure 5a (Schödel et al. 2010) reveals a second dust cavity $\sim 3''$ to the NE of the Sgr A* (drawn as a circle on Fig. 5a). The elongation and the position angles of the dust cavities are similar to the position angles of a tentative jet driven outflow from Sgr A* which was reported by Yusef-Zadeh et al. (2012). In addition, a number of resolved sources, X3, X7, F1, F2, F3, P1, P4 and the Sgr A East tower show elongated structures with similar position angles in radio and $3.8\mu\text{m}$ images (Muzic et al. 2007, 2010; Yusef-Zadeh et al. 2016). These elongated emitting features combined with elongated dust cavities, centered on Sgr A* and to the NE of Sgr A*, provide support for a common origin for the collimated outflow from Sgr A* at a position angle of $\sim 60^\circ$ (Schödel et al. 2007).

Another piece of evidence suggestive of an outflow from Sgr A* is an elongated feature from Sgr A* that curves to the SW for $\sim 5''$ and terminates in the mini-cavity. Figure 6a,b show grayscale images of the inner $4'' \times 6''$ of Sgr A* and contours of 44 GHz emission superimposed on a H-band image. The outline of the elongated edge-brightened balloon-shaped feature with a $4'' \times 1''$ extent, is drawn on Figure 6a. The northern arc-like structure of this balloon-shaped structure, as shown in Wardle and Yusef-Zadeh (1992), coincides with a blob known as “epsilon” (Yusef-Zadeh et al. 1990) which has been detected in earlier low spatial resolutions at 15 GHz (Zhao et al. 1991). The new image shows clearly that the blobs are extended and continue to form a balloon in the direction of the mini-cavity. A balloon-shaped structure to the SW and a dust cavity to the NE of Sgr A* suggest that these features are related. The proper motion measurement of the ϵ blob shows high velocity ionized gas moving away from Sgr A* to the SW (Zhao et al. 2009). This morphological and kinematic information suggests that the elongated features to the NE and SW are consistent with the outflow interpretation from Sgr A*. Future

high resolution proper motion, polarization and spectral index measurements of the ridge will provide additional constraints on the claim that this feature is physically associated with Sgr A*.

3.5 Near-IR and Millimeter Astrometry

Given the accurate position of Sgr A* at radio wavelength (Reid et al. 1999; Choate and Yusef-Zadeh 1999), we investigated if there were any positional shifts between the peak mm and radio emission from Sgr A*. The detection of several stellar sources and the magnetar at both radio and mm wavelengths in the same epoch provides a means of registering the Galactic center at radio and near-IR frames. We calibrated the images astrometrically by using the common positions of sources listed in Table 1. The positions in the near-IR images were measured via Gaussian fitting in AIPS. The astrometry was solved with the IDL solve-astro routine from ASTROLIB. No distortion solution was fitted, instead the linear terms were utilized, which involves slight shifts that exist between the 2 frames (VLT vs VLA). The VLT image was shifted in RA and Dec by 1.14 and 0.99 pixels with a pixel size of 29.033 milliarcseconds (mas). The rms scatter was 0.40 and 0.71 amongst the sources. While the VLA data should intrinsically have very good absolute pointing, the sources are so faint that the centroids of each source are fairly uncertain. The WCS coordinates of the VLT image were then modified to adjust for the shifts. The RA/Dec coordinates of the common sources were then computed which resulted in a better agreement to the VLA frame.

We included the uncertainty of the position of six stellar sources detected in both 226 (the first epoch) and 44 GHz in the computation to register self-calibrated VLA and ALMA images. The pointing center of ALMA observations was set at $\alpha, \delta(J2000) = 17^h 45^m 40^s.040, -29^\circ 00' 28''.2$. After calibrating the data using CASA and applying self-calibration gains, the peak position of Sgr A* is $\alpha, \delta(J2000) = 17^h 45^m 40^s.040004, -29^\circ 00' 28''.1997$. The computed shifts that the 226 GHz image needed to register radio and mm sources are -0.6524 and -5.821 pixels with $29.033 \text{ mas pixel}^{-1}$. We obtained the astrometrically-corrected position of Sgr A* at 226 GHz and determined that it is $3.37 \pm 0.04 \text{ mas}$ to the east and $11.03 \pm 0.23 \text{ mas}$ to the north of the radio position, thus the centroid of Sgr A* at 226 GHz is shifted by $11.53 \pm 0.23 \text{ mas}$ NE of the radio position at 44 GHz. This positional shift estimate assumes that the sources of ionized winds are symmetrical at 44 and 226 GHz, thus there is no optical depth effect that can be significant to explain the appearance of a shift in the position of Sgr A*.

Given that interstellar scattering is much smaller at 226 GHz than at 44 GHz, the origin of the positional shift between radio and mm is not clear but it is likely that Sgr A* is contaminated by a strong mm source that shifts the bright position of Sgr A*. The source is resolved in Table 2 based on our second observation on 2016, July 18. The deconvolved angular size from our first epoch observation 2016, July 12 is $0.015'' \times 0.013''$ (PA= $122 \pm 30^\circ$). If the linear ridge in Figure 2b becomes brighter close to the peak of Sgr A* at 226 GHz, it might be responsible for the shift. If so, this jet-like linear ridge arising from Sgr A* must have a hard or highly inverted spectrum since there is no significant emission detected at lower frequencies. In fact, recent high resolution 86 and 230 GHz observations of Sgr A* with milliarcsecond resolutions show an asymmetric source structure (Brinkerink et al. 2016; Fish et al. 2016). This secondary component has a position angle PA $\sim 90^\circ$ and is shifted $100 \mu\text{as}$ to the east of the main source. This asymmetry could be explained by interstellar scattering effects or intrinsic to the source (Brinkerink et al. 2016). The positional shifts in these and VLBA measurements with vastly different spatial resolution suggests that they may be physically associated with each other and that the asymmetric source structure of Sgr A* is likely to be an intrinsic jet-like source emitted in the east-west direction before gets redirected to the northeast.

3.6 Radial Fibrils of mm Emission

One of the striking features we note in the mm images of the Galactic center are faint linear features with an extent ranging between 2 and $10''$. The widths of these narrow features, which we call fibrils, are unresolved spatially and their typical intensity is $\sim 50\text{-}100 \mu\text{Jy beam}^{-1}$ above the background. Figure 7a points to seven fibrils that are tentatively detected mainly to the NW and SW of Sgr A* at 226 GHz. Figures 7b with a slightly lower spatial resolution shows the innermost region of Figure 7a where radial fibrils are mainly found in the direction away from the Galactic center. Although weak linear features in complex radio images of Sgr A* can be problematic, it is difficult to see how the linear features in ALMA images could be artifacts. This is because of the geometry of the array which is has a spiral pattern unlike the linear configuration of the VLA. We also note that some of the fibrils appear to terminate at compact sources identified as radio and mm mass-losing young star to the SW of Sgr A*. Figure 8a shows a blow-up image of the region in reverse color where a network of fibrils with strongest emission is detected. The lines *a* to *d* are drawn parallel to the PA of individual fibrils. The best example of these

faint sources with a varying background is *b*. Fibrils *c* and *d* appear to arise from stellar windy sources AF and AFNW. We also compared the mean value of the region where fibrils are detected in the region immediately to the east where there is no evidence of fibrils; the comparison showed a six-time-increase in the mean flux density of the region where fibrils are detected but the rms value was $0.1 \text{ mJy beam}^{-1}$ in both regions. Another indication of the fibrils, along the line *c* in Figure 8a, can be seen in Figure 8b showing a linear feature in the direction away from AF/HH with an extent of $20''$. In order to bring out the weak and extended tail behind the AF star, the brightness of the mini-spiral is saturated. A schematic diagram of Figure 9 shows the faint fibrils as well as the dust and molecular layers (in black) associated with the mini-spiral. Given these caveats, sensitive measurements are clearly needed to confirm the tentative detection of fibrils described here.

4 DISCUSSION

4.1 Low Extinction Millimeter Halo

Chandra observations have characterized the X-ray emission surrounding Sgr A* as spatially extended with a radius of $\sim 1.5''$ (Baganoff et al. 2003; Wang et al. 2013; Rozanska et al. 2015). The X-ray luminosity is interpreted in terms of a radiatively inefficient accretion flow (RIAF, e.g. Yuan et al. 2004; Moscibrokzka et al. 2009). In this model, a fraction of the gaseous material accretes onto Sgr A* and the rest is driven as an outflow from Sgr A* (e.g., Quataert 2004; Shcherbakov and Baganoff 2010; Wang et al. 2013). Alternatively, the diffuse X-ray emission associated with Sgr A* is interpreted as an expanding hot wind produced by the mass-loss from B-type main sequence stars, and/or the disks of photoevaporation of low mass young stellar objects (YSOs) at a rate $\sim 10^{-6} M_{\odot} \text{ yr}^{-1}$ (Yusef-Zadeh et al. 2016). The new millimeter halo emission and a dust cavity provide additional constraints on the origin of the gas in the inner $1''$ of Sgr A*.

The millimeter halo is coincident with the X-ray emission around Sgr A*, which is dominated by bremsstrahlung arising from a medium with $n_e \sim 150 \text{ cm}^{-3}$ and $T \sim 3 \times 10^7 \text{ K}$. The bremsstrahlung contribution at 230 GHz, about $0.2 \mu\text{Jy}$, is negligible. Thermal continuum from dust can also be ruled out because of the halo's extinction deficit of 0.5 magnitudes at H-band relative to its surroundings. The millimeter emission could, however, be produced by synchrotron emission from relativistic electrons in equipartition with a $\sim 1.5 \text{ mG}$ magnetic field. The energy density of each of these components would then be $\sim 10\%$ of the thermal energy density of the hot gas, so this is plausible. The luminosity in the mm is $4\pi d^2 \nu S_{\nu} \sim 1.4 \times 10^{33} \text{ ergs}^{-1}$, comparable to the X-ray luminosity, $L_X \sim 1 \times 10^{33} \text{ ergs}^{-1}$, implying that synchrotron cooling is marginally the dominant cooling mechanism for the gas. The synchrotron cooling time is $\sim 1000 \text{ yr}$, cf. the hot gas cooling time $\sim 10^5 \text{ yr}$, so this requires electron acceleration on this time scale.

The coexistence of synchrotron emission with the hot gas supports a scenario in which the gas is produced by the interaction of winds either from the S-stars or by the photo-evaporation of low-mass YSO disks (Yusef-Zadeh et al. 2016). In this picture the high relative speed of the orbital motion of the sources means that the gas is shocked to keV temperatures even though the outflow velocity from the sources is low. These shocks would also accelerate relativistic electrons. In steady state, the rate of conversion of kinetic energy to heat and relativistic electrons in shocks should equate to the X-ray and mm luminosities, respectively, therefore they should be approximately equal.

An alternative scenario is that outflow from the vicinity of Sgr A* has created an X-ray/mm bubble in a denser medium. The extinction deficit $A_K \approx 0.5$ associated with the bubble is equivalent to a “missing” column density $\sim 10^{22} \text{ cm}^{-2}$, or a number density $n_H \sim 3 \times 10^4 \text{ cm}^{-3}$. The current pressure inside the bubble would drive expansion at a speed of $\sim 40 \text{ km s}^{-1}$ into such a medium, yielding an expansion time scale of $\sim 1300 \text{ yr}$.

One possible origin of the outflow is from mass-losing evolved and/or young stars. Because of the inverted spectrum of mass-losing stars the emission is stronger at higher frequencies. Assuming a typical flux density $\sim 1 \text{ mJy}$ at 226 GHz, a total of 80 stars are needed to account for the diffuse emission. So, in this picture, the diffuse millimeter emission should resolve into individual stars with stellar winds. Because of the high orbital motion of stars and higher mass loss rates, $\sim 10^{-7} - 10^{-6} M_{\odot} \text{ yr}^{-1}$ from recent modeling (Offner & Arce 2015), the X-ray gas is supplied by shocked winds. Similar to mm emission, X-ray emission should be resolved into individual stellar sources. One possibility is enhanced X-ray emission at about $1.06''$ from the peak X-ray emission from Sgr A*. This emission appears to coincide with IRS 16C.

In summary, we have presented a variety of structures within $30''$ of Sg A* (see the diagram in Figure 9) using data taken with the VLA and ALMA. On the smallest scale, we detect 226 GHz emission from a $2.5'' \times 1.5''$ halo

that appears to coincide with a dust cavity and diffuse X-ray gas centered on Sgr A*. This mm emission coincides with diffuse X-ray emission centered on Sgr A*. We argued that the mm emission is due to synchrotron, generated either from fast-moving orbiting stars or protostars or from the activity associated with Sgr A*. This implies an outflow that produced the mm and X-ray emission and destroyed dust grains. On a scale of 5'' from Sgr A*, we detect elongated balloon-shaped structure and a dust cavity that are roughly in the direction where a number of head-tail radio sources are found in previous measurements. These morphological details can be described by a collimated outflow from Sgr A* at a position angle of 60°. We also detected mm emission from ionized winds of massive stars orbiting Sgr A* and determined their spectral indices. Lastly, we found a discrepancy in the peak position of Sgr A* between radio and 226 GHz. Future high frequency ALMA observations should be able to place a better constraint on frequency-dependent position of Sgr A* and to confirm tentative detection of a network of faint fibrils distributed throughout the inner 15'' of the Galactic center.

Acknowledgments: We thank the referee for excellent comments. This work is partially supported by the grant AST-0807400 from the NSF and the European Research Council under the European Union's Seventh Framework Program (FP/2007-2013). The research leading to these results has received funding from the European Research Council under the European Union's Seventh Framework Program (FP7/2007-2013) / ERC grant agreement number 614922] and by an Outside Studies Program Fellowship awarded to Macquarie University. The National Radio Astronomy Observatory is a facility of the National Science Foundation, operated under a cooperative agreement by Associated Universities, Inc.

REFERENCES

- Baganoff, F. K., et al. 2003, *ApJ*, 591, 891
 Boehle, A., Ghez, A. M., Schödel, R., et al. 2016, *ApJ*, 830, 17
 Brinkerink, C. D., Müller, C., Falcke, H., et al. 2016, *MNRAS*, 462, 1382
 Cotton, W. D. 2008, *PASP*, 120, 439
 Eckart, A., Horrobin, M., Britzen, S., et al. 2014, *The Galactic Center: Feeding and Feedback in a Normal Galactic Nucleus*, 303, 269
 Eckart, A., Mu Vzić, K., Yazici, S., et al. 2013, *A&A*, 551, A18
 Fish, V. L., Johnson, M. D., Doeleman, S. S., et al. 2016, *ApJ*, 820, 90
 Genzel, R., Eisenhauer, F., & Gillessen, S. 2010, *Reviews of Modern Physics*, 82, 3121
 Gillessen, S., Eisenhauer, F., Fritz, T. K., et al. 2009, *ApJ*, 707, L114
 Gillessen, S., Genzel, R., Fritz, T. K., et al. 2012, *Nature*, 481, 51
 Gillessen, S., Plewa, P. M., Eisenhauer, F., et al. 2017, *ApJ*, 837, 30
 Kennea, J.A., Burrows, D.N., Kouveliotou, C., Palmer, D.M., et al. 2013, *ApJ*, 770, L24
 Lu, J. R., Ghez, A. M., Hornstein, S. D., et al. 2009, *ApJ*, 690, 1463
 Markoff, S., Bower, G. C., & Falcke, H. 2007, *MNRAS*, 379, 1519
 Mu Vzić, K., Eckart, A., Schödel, R., et al. 2010, *A&A*, 521, A13
 Mu Vzić, K., Eckart, A., Schödel, R., Meyer, L., & Zensus, A. 2007, *A&A*, 469, 993
 Offner, S. S. R., & Arce, H. G. 2015, *ApJ*, 811, 146
 Panagia, N. 1973, *AJ*, 78, 929
 Panagia, N., & Felli, M. 1975, *A&A*, 39, 1
 Paumard, T., Genzel, R., Martins, F., Nayakshin, S., Beloborodov *et al.* 2006, *ApJ*, 643, 1011
 Pfuhl, O., Gillessen, S., Eisenhauer, F., et al. 2015, *ApJ*, 798, 111
 Pott, J.-U., Eckart, A., Glindemann, A., et al. 2008, *A&A*, 480, 115
 Quataert, E. 2004, *ApJ*, 613, 322
 Reid, M. J., & Brunthaler, A. 2004, *ApJ*, 616, 872
 Reid, M. J., Readhead, A. C. S., Vermeulen, R. C., & Treuhaft, R. N. 1999, *ApJ*, 524, 816
 Różańska, A., Mróz, P., Mościbrodzka, M., Sobolewska, M., & Adhikari, T. P. 2015, *A&A*, 581, A64
 Shcherbakov, R. V., & Baganoff, F. K. 2010, *ApJ*, 716, 504
 Schödel, R., Najarro, F., Muzic, K., & Eckart, A. 2010, *A&A*, 511, A18
 Schödel, R., Eckart, A., Alexander, T., et al. 2007, *A&A*, 469, 125
 Schödel, R., Feldmeier, A., Kunneriath, D., et al. 2014, *A&A*, 566, A47
 Shannon, R. M., & Johnston, S. 2013, *MNRAS*, 435, L2
 Torne, P., Desvignes, G., Eatough, R. P., et al. 2017, *MNRAS*, 465, 242
 Valencia-Schneider et al. 2015, *ApJ*, 800, 125
 Viehmann, T., Eckart, A., Schödel, R., et al. 2005, *A&A*, 433, 117
 Wang, Q. D., Nowak, M. A., Markoff, S. B., et al. 2013, *Science*, 341, 981
 Wardle, M., & Yusef-Zadeh, F. 1992, *Nature*, 357, 308
 Witzel, G., Ghez, A. M., Morris, M. R., et al. 2014, *ApJ*, 796, LL8
 Yelda, S., Ghez, A. M., Lu, J. R., et al. 2014, *ApJ*, 783, 131
 Yelda, S., Lu, J. R., Ghez, A. M., et al. 2010, *ApJ*, 725, 331
 Yuan, F., Quataert, E. & Narayan, R. 2004, *ApJ*, 606, 894
 Yusef-Zadeh, F., Diesing, R., Wardle, M., et al. 2015, *ApJ*, 811, L35

- Yusef-Zadeh, F., Wardle, M., Sewilo, M., et al. 2015, ApJ, 808, 97
Yusef-Zadeh, F., Bushouse, H., Schödel, R., et al. 2015, ApJ, 809, 10
Yusef-Zadeh, F., Wardle, M., Schödel, R., et al. 2016, ApJ, 819, 60
Yusef-Zadeh, F., Roberts, D., Heinke, C., et al. 2014b, The Astronomer's Telegram, 6041, 1
Yusef-Zadeh, F., Cotton, W., Wardle, M., et al. 2017, MNRAS,
Yusef-Zadeh, F., Arendt, R., Bushouse, H., et al. 2012, ApJ, 758, L11
Yusef-Zadeh, F., Roberts, D. A., Bushouse, H., et al. 2014, ApJ, 792, L1
Yusef-Zadeh, F., Choate, D., & Cotton, W. 1999, ApJ, 518, L33
Yusef-Zadeh, F., Morris, M., & Ekers, R. D. 1990, Nature, 348, 45
Zhao, J.-H., Goss, W. M., Lo, K. Y., & Ekers, R. D. 1991, Nature, 354, 46
Zhao, J.-H., Morris, M. R., Goss, W. M., & An, T. 2009, ApJ, 699, 186

This paper has been typeset from a \TeX/L\AA\TeX file prepared by the author.

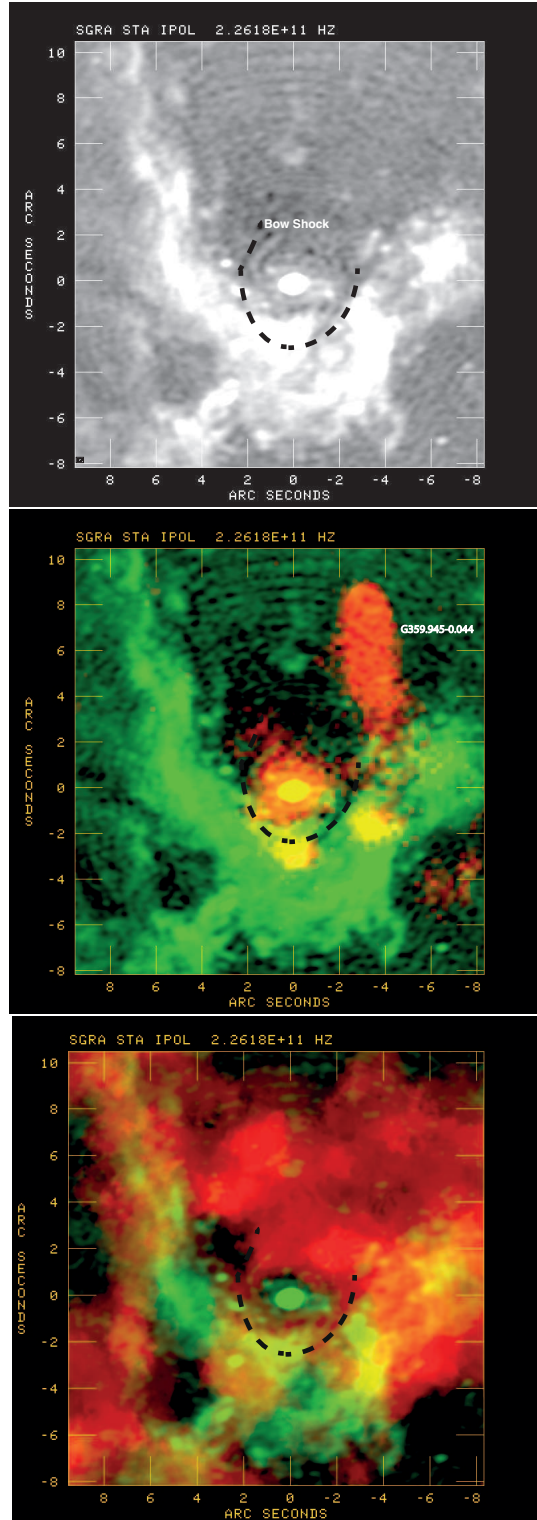


Figure 1. (a) A 226 GHz image of the mini-spiral with spatial resolution of $0.38'' \times 0.27''$ and PA= -79° . This image is based on combining both observations taken in two epochs on 2016, July 12 and 18. The peak flux is $3.47 \text{ Jy beam}^{-1}$. (The grayscale range $-6.7 \times 10^{-4} - 3 \times 10^{-3} \text{ Jy beam}^{-1}$.) (b) Similar to (a) except that an X-ray 1.5-7 keV image in red taken with Chandra (D. Haggard, private communication) is superimposed on a 226 GHz image in green. (The grayscale range 0 to 10^4 counts.) $-6 \times 10^{-4} - 3 \times 10^{-3} \text{ Jy beam}^{-1}$.) (c) Similar to (a) except the Ks extinction image (Schödel et al. 2010) in red is superimposed on a 226 GHz image in green. The range of extinction value is between 2.35 and 3.20 magnitudes. (The grayscale range $-6.7 \times 10^{-4} - 1 \times 10^{-2} \text{ Jy beam}^{-1}$.)

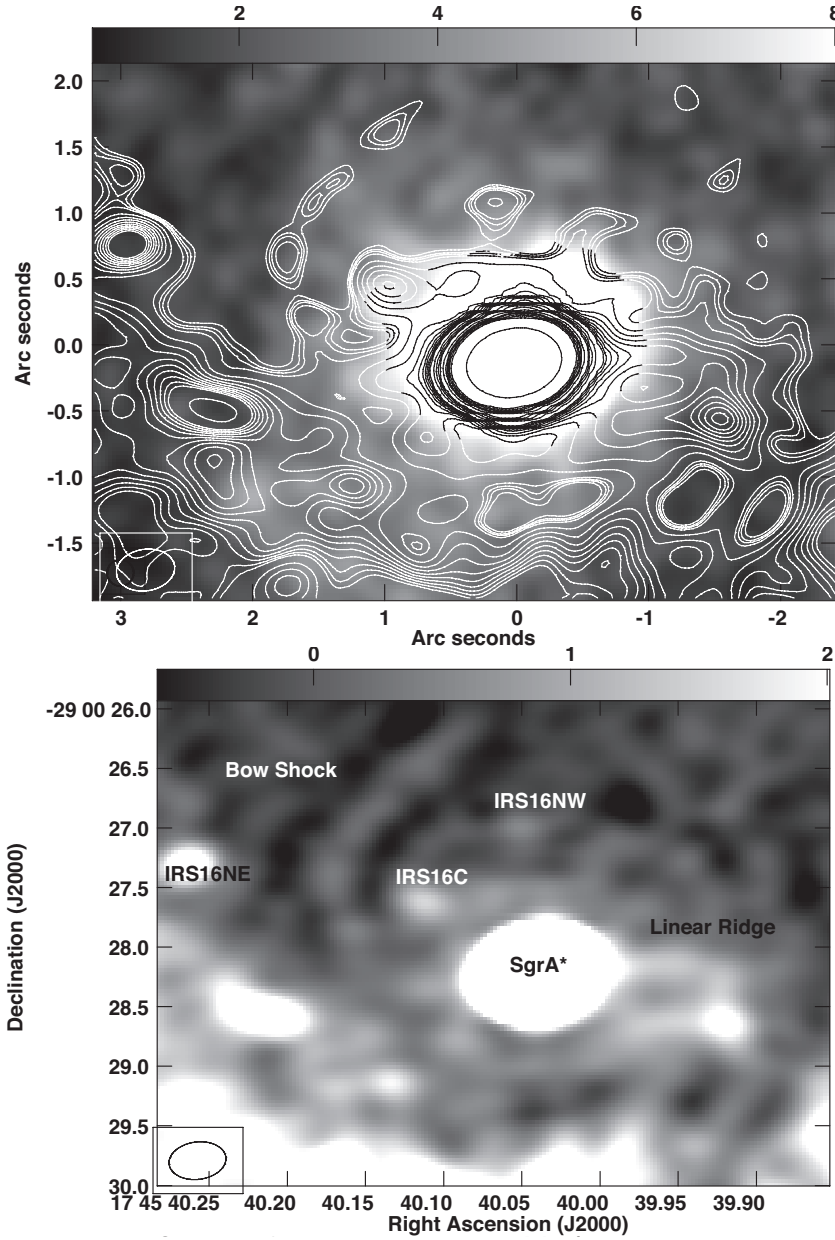


Figure 2. (a) Contours of 226 GHz emission with levels set at (1, 2,...,10, 12, 15, 20, 25, 30, 35, 40, 50, 55, 60, 65, 70, 80, 90, 110, 130) $\times 0.15$ mJy beam $^{-1}$ are superimposed on an 1.5-7 keV X-ray image of Sgr A* with the spatial resolution of $\sim 0.5''$. (The grayscale range 0 to 8×10^3 counts.) (b) A grayscale image of the mm emission from the inner $4'' \times 6''$ of Sgr A* with similar resolution to the 226 GHz image in (a). Prominent stellar sources, the bow shock and the linear features are labeled. (The grayscale range $-1 \times 10^{-3} - 3 \times 10^{-3}$ Jy beam $^{-1}$.)

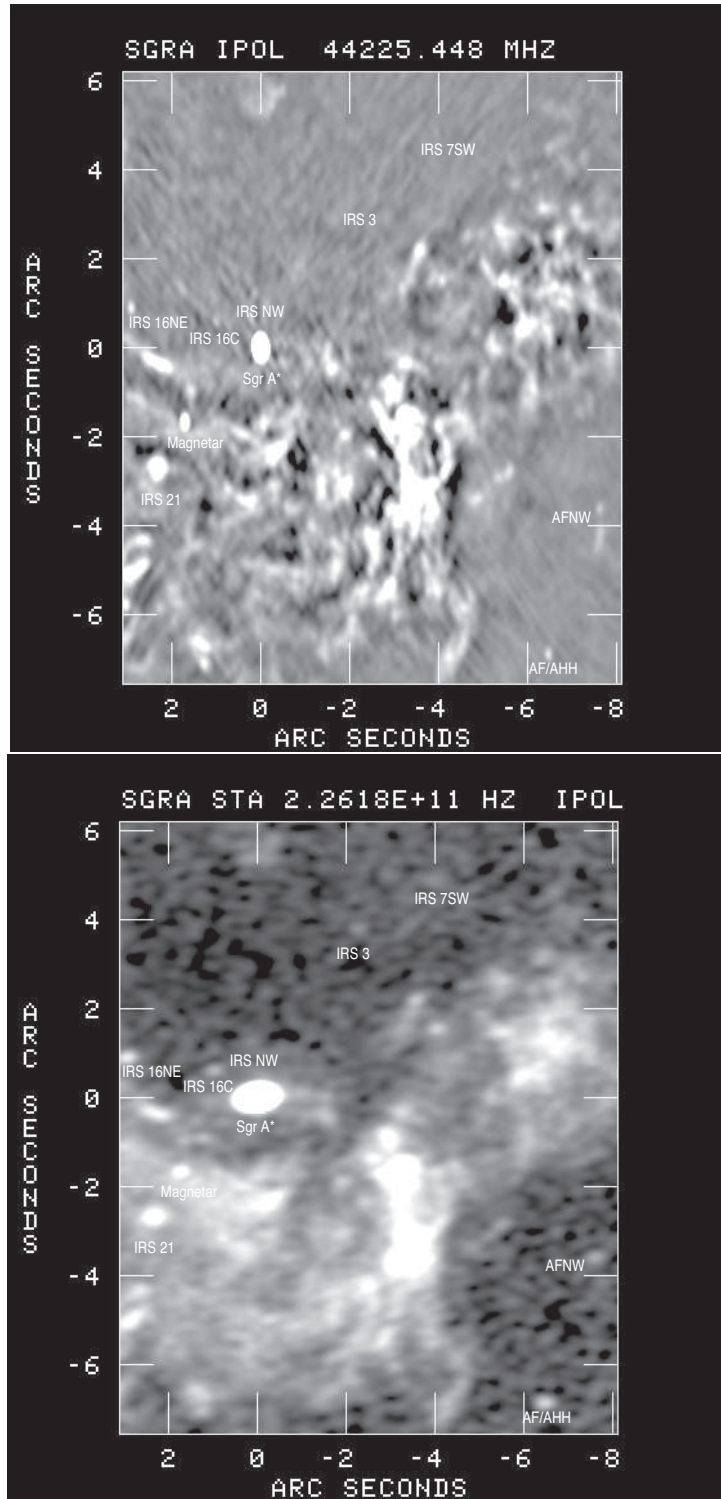


Figure 3. (a) Top A 44 GHz image of the mini-spiral is constructed by limiting the uv range to greater than $100 \text{ k}\lambda$ with a spatial resolution of $0.22'' \times 0.13''$ (PA= 3.8°) from the 2016, July 12 epoch. (The grayscale range $-5 \times 10^{-4} - 5 \times 10^{-4} \text{ Jy beam}^{-1}$.) (b) Bottom A 226 GHz image of the mini-spiral with similar resolution to that of Figure 1a. Labeled sources are compact with properties listed in Tables 1 and 2. (The grayscale range $-6.7 \times 10^{-4} - 1 \times 10^{-2} \text{ Jy beam}^{-1}$.)

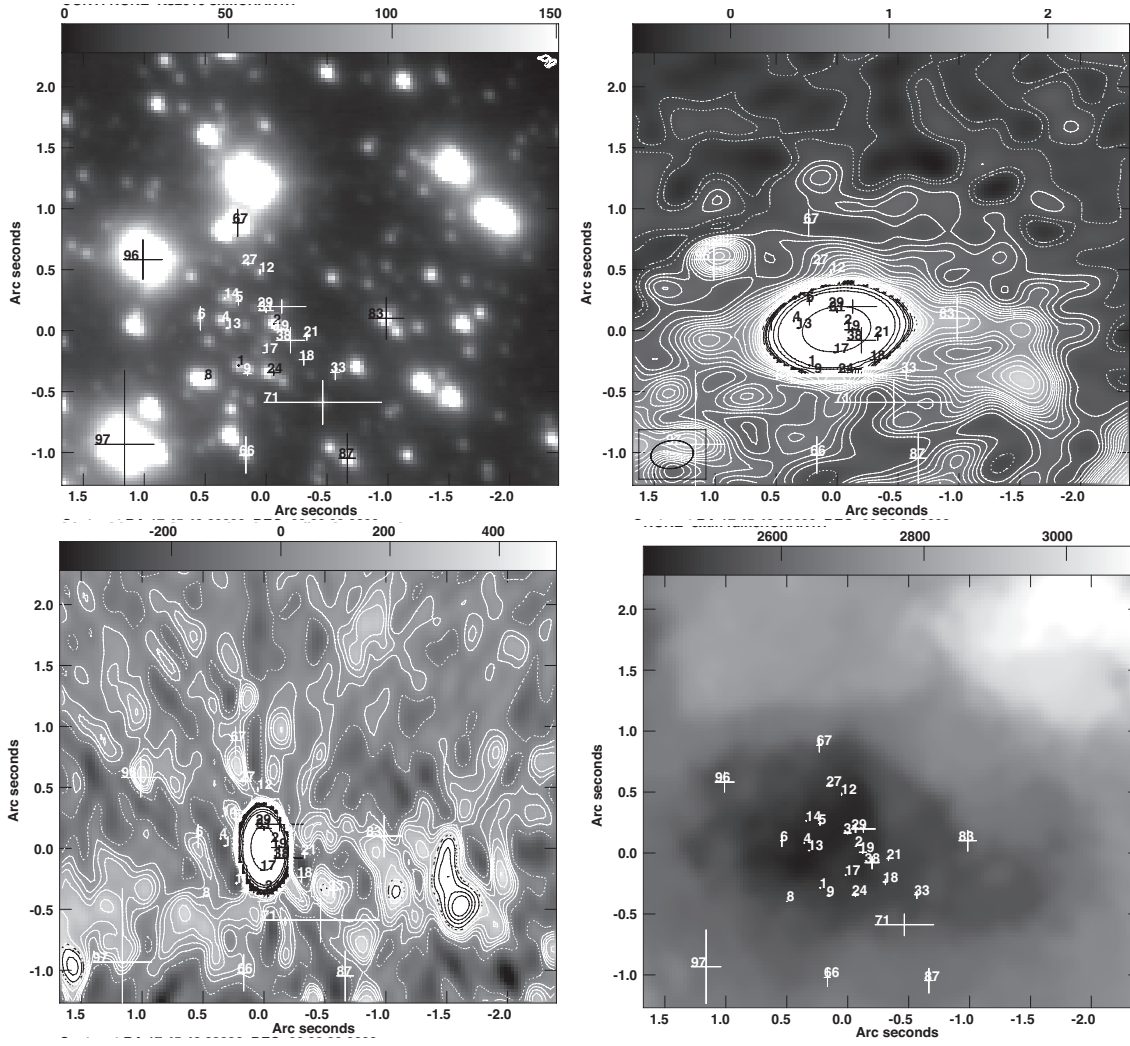


Figure 4. (a) *Top Left* A grayscale image of the inner 3.5'' of Sgr A* at H band taken on 2016, July 12. (b) *Top Right* Grayscale contours of 226 GHz emission set at $(-2, -1, 1, 2, \dots, 10, 12, \dots, 20, 25, 30, 35, 40, 50, 100, 200, 5000) \times 0.1 \text{ mJy beam}^{-1}$ with a spatial resolution of $0.35'' \times 0.23''$ (PA= -82.7°). (c) *Bottom Left* Grayscale contours of 44.2 GHz emission set at $(-2, -1, 1, 2, \dots, 10, 12, \dots, 20, 25, 30, 35, 40, 50, 100, 200, 5000) \times 0.05 \text{ mJy beam}^{-1}$ with a spatial resolution of $0.22'' \times 0.13''$ (PA= 3.8°), taken on 2016, July 12. (d) *Bottom Right* An extinction map showing an elongated dust cavity coincident with the S cluster (Schoödel et al. 2009). Stellar sources associated with the S cluster are labeled at their expected positions on 2016, July 12. The extinction ranges between 2.4 and 3.14 magnitudes.

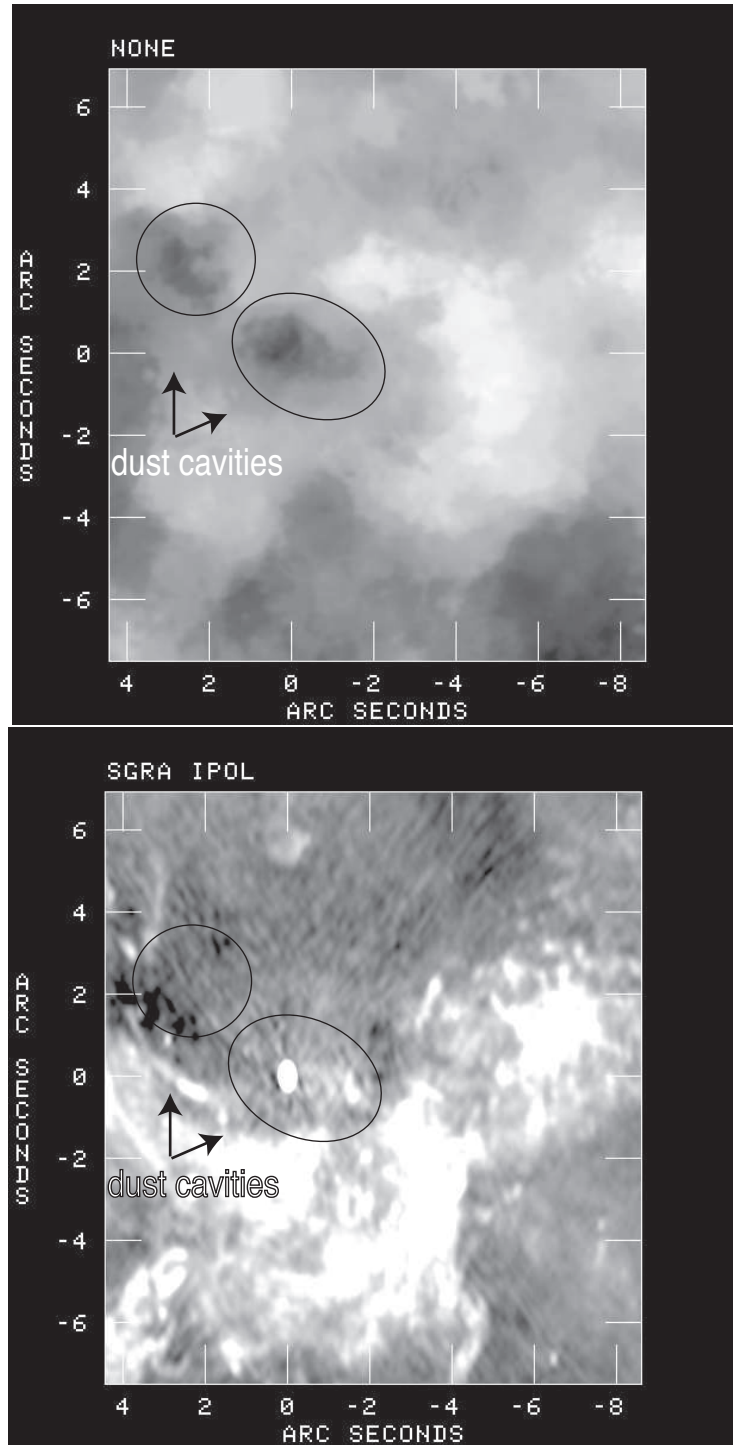


Figure 5. (a) *Top* Similar to the region shown in Figure 4d except the inner $13'' \times 13''$ of Sgr A*. The extinction ranges between 2.4 and 3.20 magnitudes. (b) *Bottom* Similar to the region shown in Figure 3a except that uv data was not truncated, resulting a spatial resolution of $0.24'' \times 0.14''$ (PA=3.3°). (The grayscale range $-3 \times 10^{-4} - 1 \times 10^{-3}$ Jy beam $^{-1}$.)

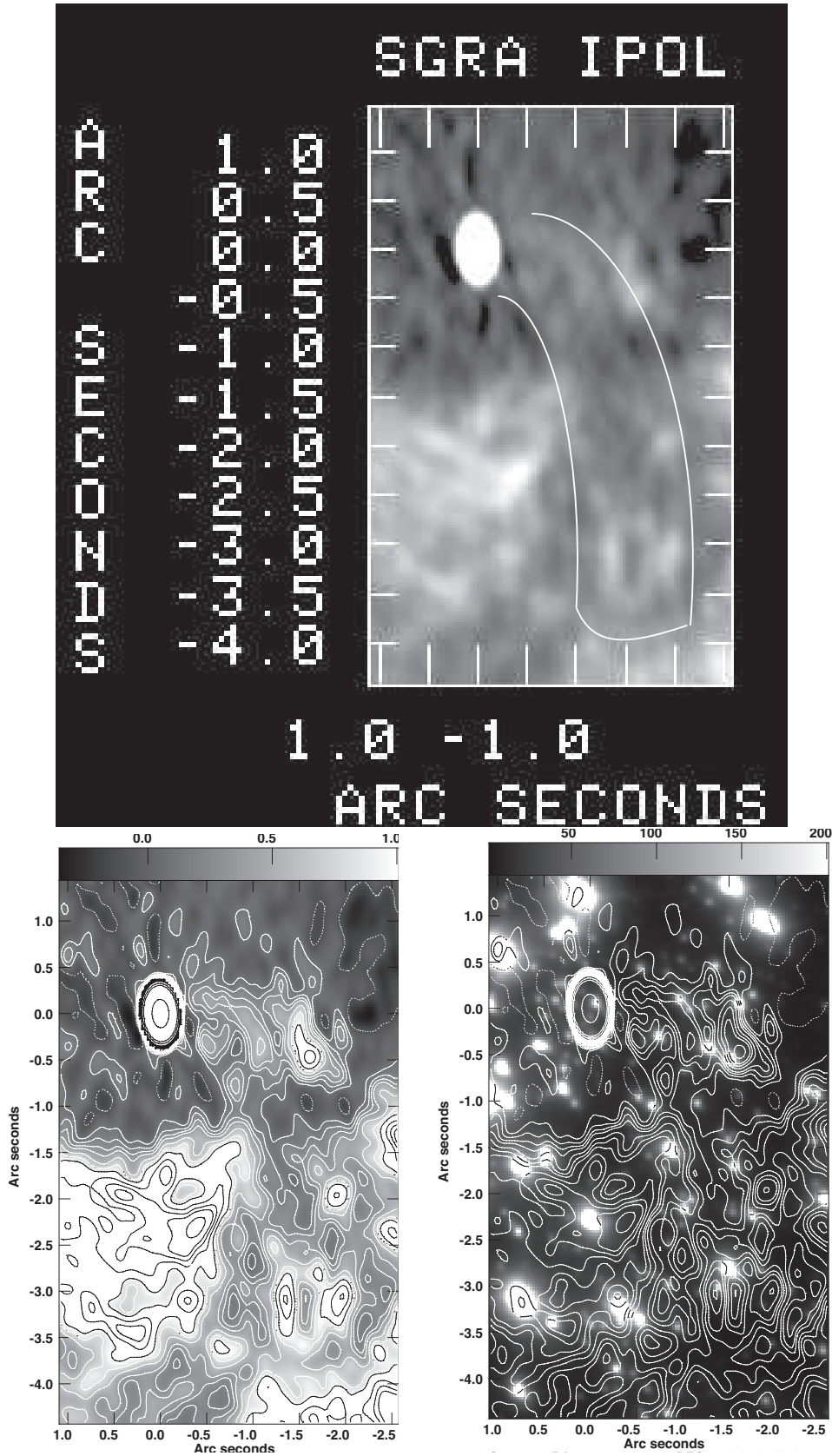


Figure 6. (a) *Top* Similar to Figure 5b except the inner $3.5'' \times 6''$ of Sgr A*. (b) *Bottom Left* Similar to (a) except showing grayscale contours of emission set at $(-2, -1, 1, 2, \dots, 10, 14, 18, 22, 30, 38, 46, 100, 200, 5000) \times 0.1 \text{ mJy beam}^{-1}$. (c) *Bottom Right* Similar to (b) except that the 44 GHz contours are superimposed on a H-band image.

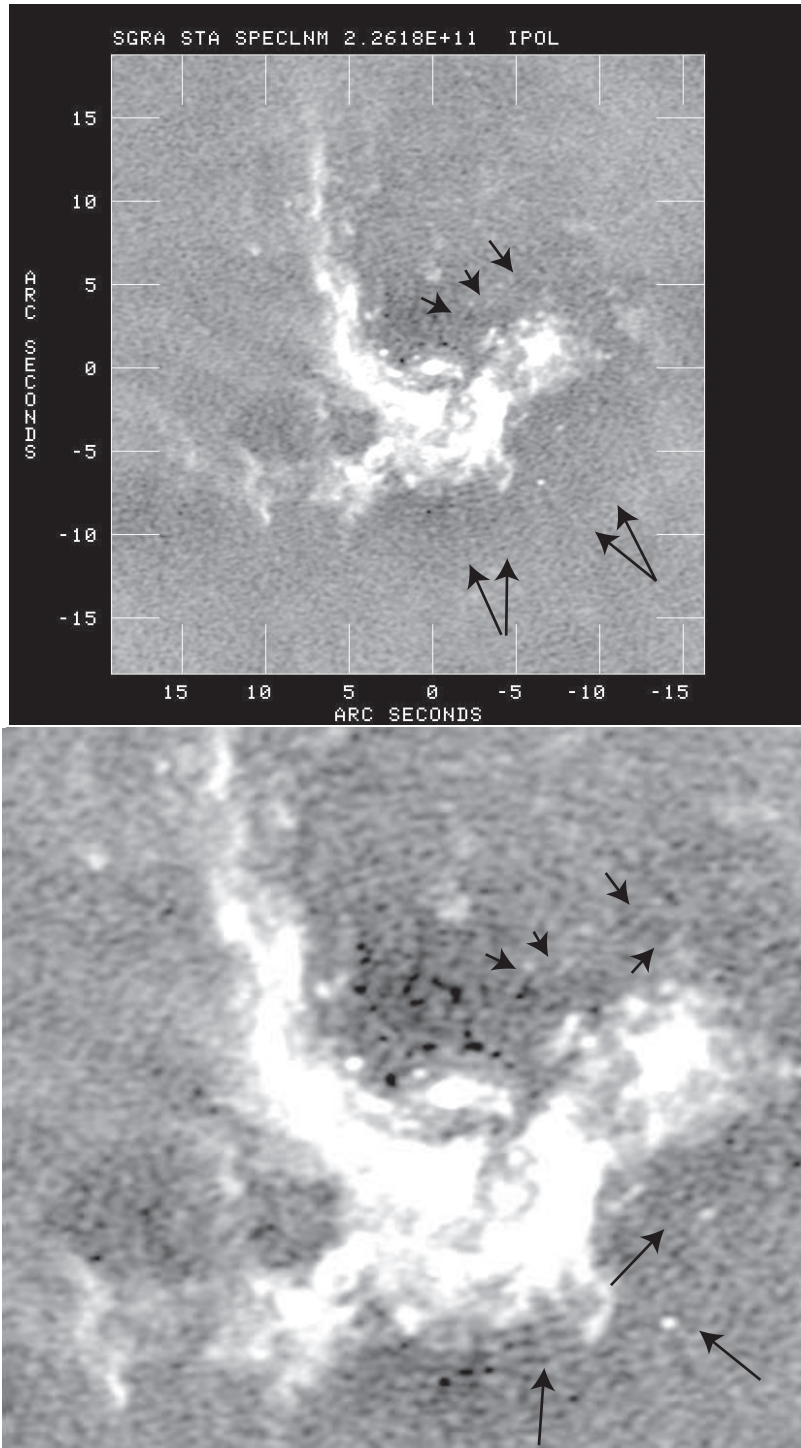


Figure 7. (a) *Top* A Grayscale 226 GHz image of the mini-spiral with a spatial resolution of $0.22'' \times 0.13''$ (PA= 3.8°) taken on 2016, July 18 with ALMA. (b) *Bottom* The inner quarter of the 226 GHz image shown in (a) with a resolution of $0.36'' \times 0.24''$ (PA= $-82^\circ.4$). The arrows point to faint fibrils detected in radio and mm images.

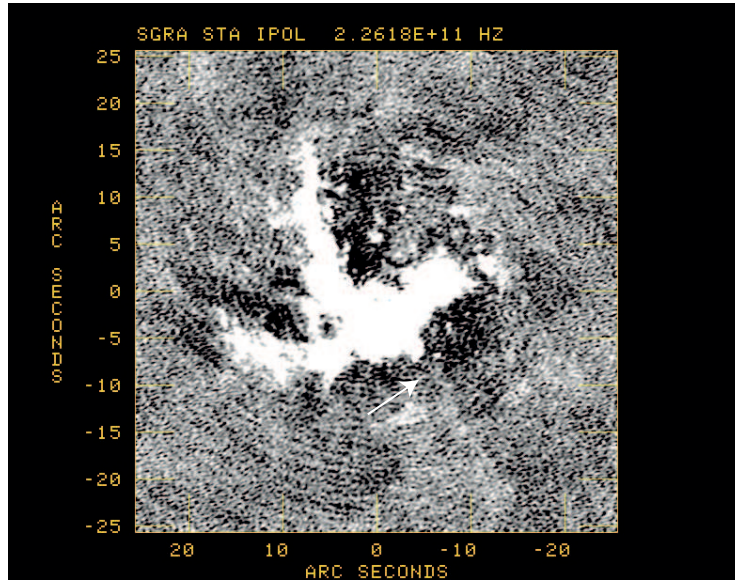
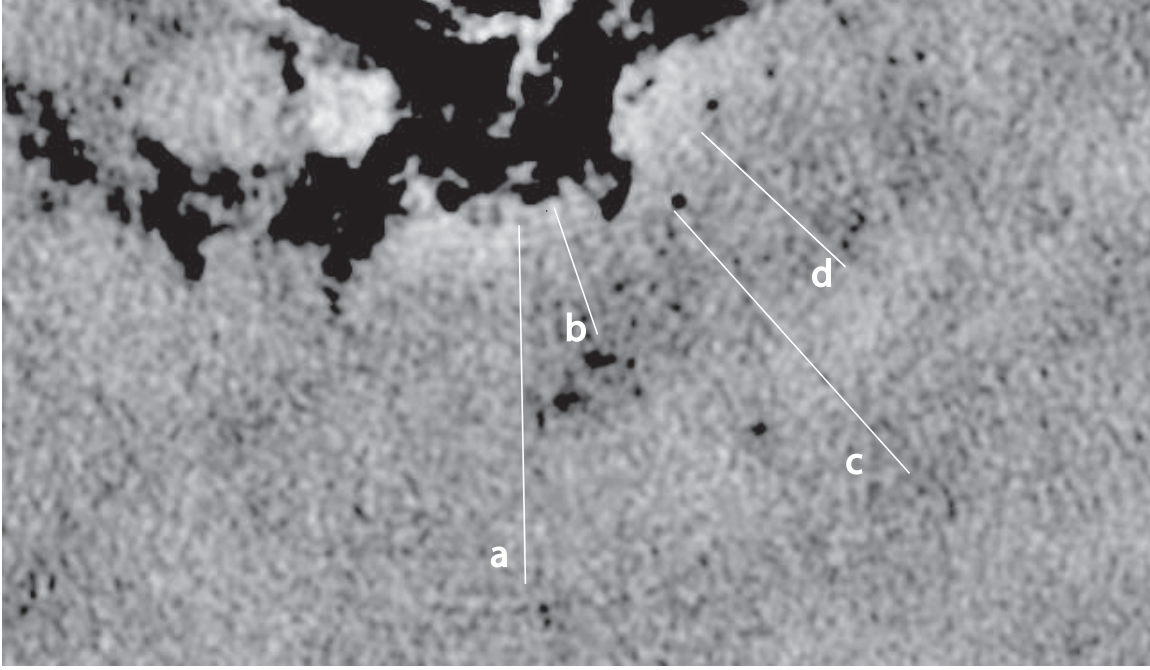


Figure 8. (a) *Top* A 226 GHz image (in reverse color) with a resolution of $0.45'' \times 0.45''$ from the 2016, July 18 data taken with ALMA. The drawn paralld lines point where the fibrils are located. (b) *Bottom* A 226 GHz image with a spatial resolution of $0.44'' \times 0.34''$ (PA= -70.8°) taken on 2016, July 12 with ALMA. (The grayscale range $-3 \times 10^{-4} - 5 \times 10^{-4}$ Jy beam $^{-1}$.)

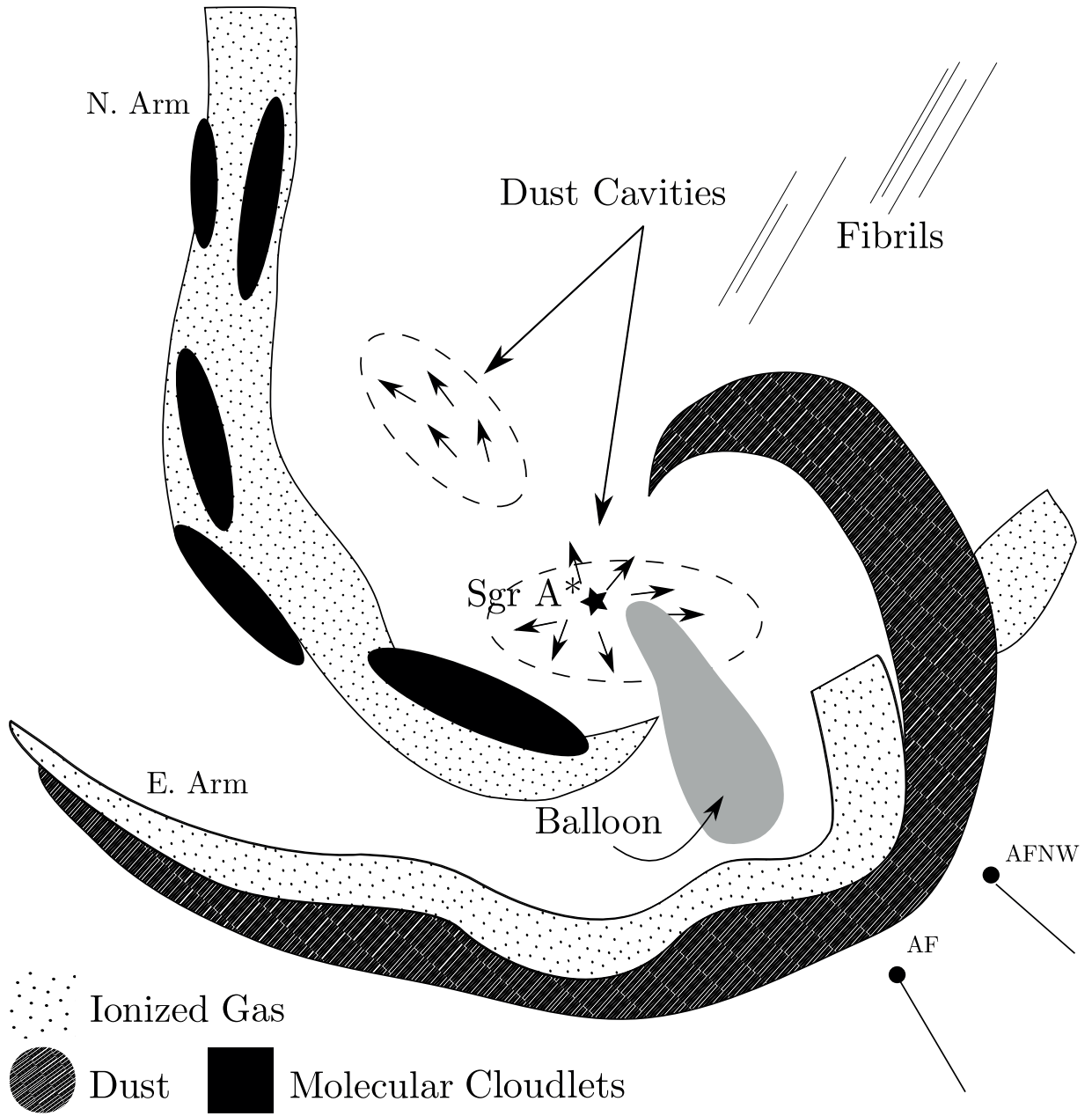


Figure 9. A schematic picture of major features found at 226 GHz. Dark features point to regions where extended dust and neutral gas is detected.

Table 1. Parameters of 2D Gaussian fits to 44 GHz Stellar Sources

ID	Alt Name	RA (J2000)	Dec (J2000)	Distance from Sgr A*	Position Accuracy	$\theta_a \times \theta_b$ (PA)	Peak Intensity	Spectral Index	Integrated Flux
		(17 ^h 45 ^m)	(−29°00′)	(arcsec)	(mas)	mas × mas (deg)	(mJy beam ^{−1})	(α)	(mJy)
1	Sgr A*	40.0383	28.0690	0.00	0.00	3 × 0 (31)	1536.400 ± 0.052	0.56 ± 0.00004	1536.900 ± 0.090
2	IRS 16C	40.1134	27.4370	1.17	12.24	193 × 155 (177)	0.502 ± 0.049	0.67±0.29	1.044 ± 0.143
3	IRS 16NW	40.0487	26.8459	1.23	16.41	109 × 0 (149)	0.317 ± 0.052	0.28±0.81	0.293 ± 0.085
4	Magnetar	40.1685	29.7421	2.39	0.88	74 × 0 (157)	5.787 ± 0.052	−0.21±0.10	5.866 ± 0.091
5	IRS 16NE	40.2608	27.1745	3.05	5.48	100 × 0 (13)	0.977 ± 0.052	0.79±0.12	1.056 ± 0.095
6	IRS21	40.2154	30.7693	3.56	1.63	258 × 236 (98)	4.049 ± 0.048	0.23±0.07	13.309 ± 0.199
7	IRS 3	39.8614	24.2147	4.50	50.24	181 × 0 (139)	0.109 ± 0.052	1.14±0.66	0.121 ± 0.096
8	IRS 7SW	39.7383	23.2063	6.26	63.47	250 × 0 (16)	0.111 ± 0.051	1.12±0.63	0.147 ± 0.107
9	AFNW	39.4558	31.6992	8.46	12.69	95 × 43 (151)	0.411 ± 0.052	0.73±0.31	0.488 ± 0.100
10	AF/AHH	39.5446	34.9672	9.46	6.60	—	0.735 ± 0.052	0.84±0.15	0.717 ± 0.088

Table 2. Parameters of 2D Gaussian fits to 226 GHz Stellar Sources

ID	Alt Name	RA (J2000)	Dec (J2000)	Dist. from Sgr A*	Pos. Accuracy	$\theta_a \times \theta_b$ (PA)	Peak Intensity	Integrated Flux
1	Sgr A*	40.0386	28.0580	0.00	0.02	40×31 (100)	2970.000 ± 0.682	3017.500 ± 1.190
2	IRS 16C	40.1115	27.4709	1.12	43.60	29×0 (143)	1.490 ± 0.682	1.396 ± 1.130
3	IRS 16NW ²	40.0484	26.8348	1.23	187.43	243×116 (174)	0.501 ± 0.660	0.767 ± 1.540
4	J1745-29	40.1700	29.7533	2.41	18.41	128×67 (156)	4.078 ± 0.679	4.699 ± 1.290
5	IRS 16NE	40.2623	27.1747	3.07	20.39	97×81 (150)	3.535 ± 0.682	3.921 ± 1.270
6	IRS 21	40.2160	30.7499	3.56	14.20	228×185 (104)	5.877 ± 0.660	9.044 ± 1.540
7	IRS 3 ²	39.8644	24.2573	4.43	101.29	93×0 (102)	0.701 ± 0.682	0.641 ± 1.110
8	IRS 7SW ²	39.7326	23.1742	6.32	129.46	408×223 (77)	0.696 ± 0.643	1.521 ± 1.940
9	AFNW	39.4577	31.6806	8.44	58.73	240×46 (130)	1.356 ± 0.670	1.771 ± 1.390
10	AF/AHH	39.5436	34.9422	9.46	25.10	166×38 (52)	2.910 ± 0.677	3.449 ± 1.320

Table 3. Predicted Positions of Young Stars in the S Cluster from Sgr A* at the 2016.54 Epoch

Source Name	RA (offset)	Dec (offset)	(σ_X)	(σ_Y)
	<i>arcsec</i>	<i>arcsec</i>	<i>arcsec</i>	<i>arcsec</i>
S1	0.2244	-0.2862	0.0161	0.0187
S2	-0.0632	0.0536	0.0012	0.0038
S4	0.3550	0.0826	0.0226	0.0103
S5	0.2259	0.2417	0.0622	0.0429
S6	0.5399	0.0996	0.1895	0.0350
S8	0.4982	-0.3972	0.0048	0.0063
S9	0.1531	-0.3513	0.0272	0.0623
S12	0.0495	0.4826	0.0385	0.0125
S13	0.3160	0.0198	0.0128	0.0273
S14	0.3391	0.2641	0.0132	0.0103
S17	0.0161	-0.1812	0.0040	0.0205
S18	-0.3088	-0.2381	0.0932	0.0719
S19	-0.1253	0.0057	0.0381	0.1234
S21	-0.3348	-0.0473	0.0644	0.0498
S24	-0.0634	-0.3448	0.0472	0.1037
S27	0.1491	0.5496	0.0256	0.0944
S29	-0.1297	0.1967	0.1094	0.3917
S31	-0.0000	0.1630	0.0340	0.1237
S33	-0.5679	-0.3434	0.1219	0.0737
S38	-0.1996	-0.0801	0.2040	0.2352
S66	0.1655	-1.0205	0.3000	0.1063
S67	0.2320	0.8833	0.2265	0.0823
S71	-0.4660	-0.5897	0.3592	0.9643
S83	-0.9859	0.0999	0.3428	0.2893
S87	-0.6667	-1.0474	0.4086	0.1390
S96	1.0095	0.5818	0.3255	0.3163
S97	1.1609	-0.9340	1.2096	0.4843